Disconnectedness: A New Moment Invariant for Multi-Component Shapes

Joviša Žunić[a], Paul L. Rosin[b], Vladimir Ilić[c,*]

[a]Mathematical Institute, Serbian Academy of Sciences and Arts, Belgrade, Serbia
[b]Cardiff University, School of Computer Science,Cardiff CF24 3AA, Wales, U.K.
[c]University of Novi Sad, Faculty of Technical Sciences, 21000 Novi Sad, Serbia

Abstract

In this paper we further develop the recent concept of multi-component shapes, which is applicable to image processing and image analysis tasks. The domain of multi-component shapes is very diverse and includes shapes that correspond to a group of objects that act together (e.g. a fish shoal), natural components of a segmented object (e.g. cells in embryonic tissues), a set of shapes corresponding to the same object appearing at different times (e.g. human gait in an image sequence), and many more.

So far, there are few methods for numerically evaluating multi-component shapes. In this paper we introduce one such method: a disconnectedness measure, that naturally corresponds to multi-component shapes, and has no analogue in single-component shape measures. The new measure depends on the number of shape components, the whole shape but also the shape of its components, on the relative size of the shape's components and their mutual position. All these are natural requirements for a "disconnectedness" multi-component shape measure. In addition, the new measure is invariant with respect to translation, rotation and scaling transformations. The measure is simple and fast to compute.

The disconnectedness measure introduced here is a generic image analysis tool. It has not been developed for a specific application. As such, it can be applied to a variety of applications. Several of them are provided in the paper, as well as synthetic examples that support a better understanding of the behavior of the new measure.

Keywords: Shape, Multi-component shapes, Moments, Moment Invariants

1. Introduction

Shape analysis is a perennial topic in computer vision, and the topic of many books [1–7]. Shape based tools for image analysis have a wide spectrum of applications: astronomy [8, 9], medicine [10], ecology [11], botany [12], agriculture [13], archaeology [14], transport [15], particle analysis [16], technology [17, 18], just to mention a few. This is because shape has a high discriminative capacity, and shape properties can be evaluated numerically. Different approaches have been applied to characterize shapes numerically. Some of them are generic ones [19–22], aimed to satisfy some specific properties (like rotational [19, 22] or affine [21, 23] invariance, for example). There are also approaches designed to measure specific shape properties. Shape convexity [24–26], circularity [27, 28], squareness [29], tortuosity [30], ellipticity [8, 31–33], are examples of shape properties which have been studied and numerically evaluated so far. Some methods for measuring shape properties are quite old [32], while others are recent [34].

*Corresponding author.
Email addresses: jovisa_zunic@mi.sanu.ac.rs (Joviša Žunić), Paul.Rosin@cs.cf.ac.uk (Paul L. Rosin), vlada.mzsvi@uns.ac.rs (Vladimir Ilić)

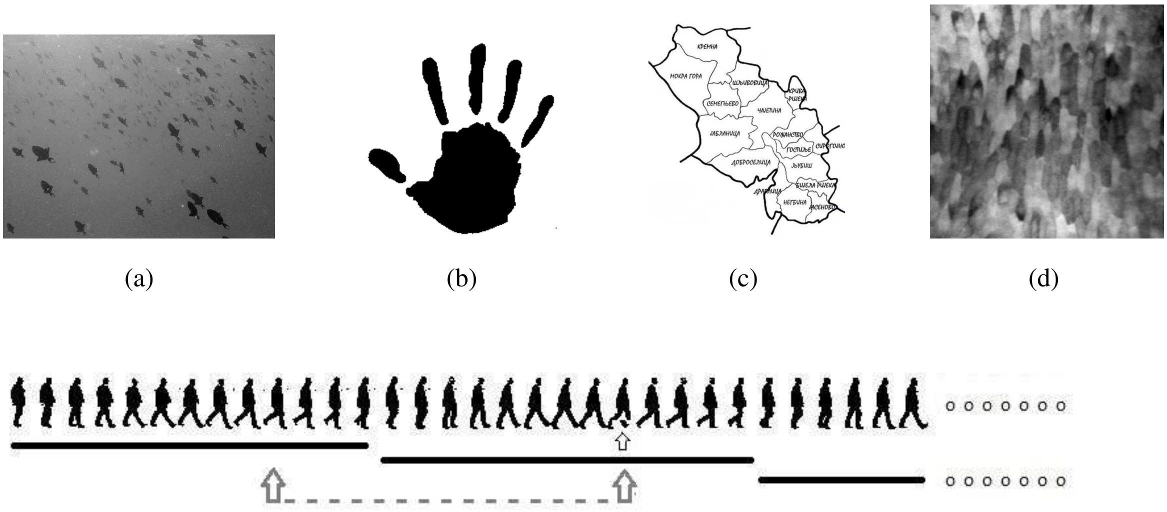

(a) (b) (c) (d)

(e)

Figure 1: (a) Fish shoal (b) Palm-print (c) Zlatibor-region partitioned by the village districts (d) Embryonic tissue with indistinct cell boundaries (e) Human gait – considered as a 13-component shape, whose components are the appearances of a walking person in a sequence of 13 consecutive frames.

Also, a range of different methodologies have been applied: algebraic [19], geometric [35], logical [36], fractal [37], and so on.

In this paper we further develop the fairly new concept of multi-component shapes [38, 39]. The concept differs essentially from the existing ones, even if it might be understood as a natural one. Multi-component (i.e. compound) shape is a very generic term. It may relate to: **(i)** Shapes corresponding to a group of the objects that act together; for example, a fish shoal, in which each single fish shape is a component of a multi-component fish-shoal shape (see Fig.1(a)). **(ii)** Shapes corresponding to an object partitioned on a natural way; an example could be a hand, whose components are the fingers and palm (Fig.1(b)). **(iii)** Shapes partitioned by criteria not directly or easily visible from an image; an example is a region (e.g. state, country, continent, etc.) divided according to some administrative criteria [40] (Fig.1(c)). **(iv)** Shapes partitioned with indistinct boundaries, but which still produce relatively naturally recognizable components (Fig.1 (d)). **(v)** Shapes whose components are the shapes of the same object appearing on consecutive sequence of frames (Fig.1(e)). Of course, there are many more examples. Some of them can be found in Section 4, related to the experiments.

Being a conceptually new approach, the multi-component shape approach has specific demands. Indeed, even a basic shape feature, such as the shape orientation of multi-component shapes, has additional requirements that do not appear when working in the domain of single-component shapes. For example, in the case of multi-component shapes that consist of a huge number of components (e.g. as a fish-shoal does), the computed orientation of such a multi-component shape should be not depend on what portion of the multi-component shape has been captured in the image frame.

In the example of the image in Fig.2, multi-component shape orientation (represented by shorter dark blue arrows) is computed for both the whole image (Fig.2b) and also separately for its left and right halves (Fig.2a). It can be seen that these three computed orientations coincide, which is the preferred outcome, and suggests that the multi-component orientation exists and is an inherent property of the given fish-shoal shape. If the whole shape and its halves are treated as single component shapes (such that all the black pixels in that portion of the image belong to the shape), then the orientations computed (represented

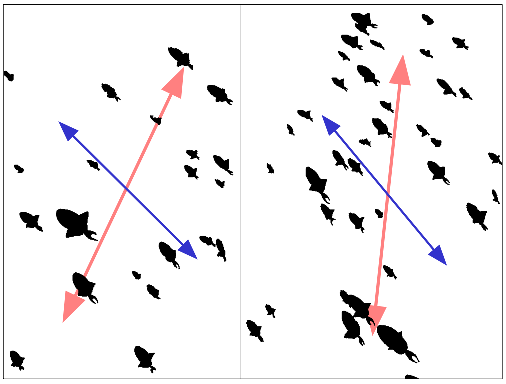

(a)

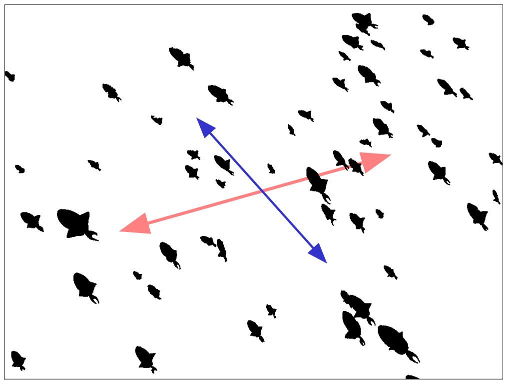

(b)

Figure 2: Orientations computed for (a) the separate left and right halves of the image, and also for (b) the complete image. Shorter dark blue arrows correspond to the shape orientations computed for the three sets of data according to our multi-component approach. In comparison, the long light red arrows correspond to the traditional method for computing orientation, in which each of the three sets of data are considered as representing single-component shapes (each containing multiple fish).

by long light red arrows) differ substantially, as these represent the global pattern rather than its contents; for more details see [39].

In this paper we introduce a new shape measure for multi-component shapes. It is named the *disconnectedness of multi-component shapes* or, for short, just the *disconnectedness measure*. The name comes from an intuitive interpretation of what the properties of a disconnectedness measure (of multi-component shapes) should satisfy. It ranges through the interval $[0,\infty)$ and returns the smallest possible value (equal to zero) for single component connected shapes. The new measure depends on the number of components, their mutual position (including the mutual distances among them) and relative sizes, the shape of the components and the shape of the whole multi-component shape considered. This will be illustrated and clarified with a number of synthetic experiments. Finally, the disconnectedness measure is invariant with respect to rotation, translation, and scaling transformations.

In our derivation we have started with the interpretation of the first Hu moment invariant [19][1], in the case of multi-component shapes. Neither an algebraic reasoning, applied in [19], nor geometric reasoning from [35], were suitable for such an extension from single-component shapes to the multi-component-ones. Another interpretation of the first Hu moment invariant, derived in this paper, has led to good arguments to derive a new measure for multi-component shapes. This measure is a generic one, not designed for a particular application. This has been demonstrated with applications on different shape based image processing tasks, provided in this paper.

Naturally, each multi-component shape measure is expected to be dependent on the components of the shape. An attempt to expand the Hu moment invariants to the multi-component shapes was carried out in [41]. Different ideas of the averaging of the component values of the corresponding Hu invariants was applied and used in a leaf classification task. To the authors' best knowledge, there is just one more measure defined so far for multi-component shapes. This is the anisotropy measure [38], whose role is to evaluate the degree to which the components of a multi-component shape are oriented consistently.

The paper is organized as follows. The basic terms and notation are in the next section. Section 3 gives a new interpretation of the first Hu moment invariant. This interpretation expresses the first Hu moment invariant, of a single component shape, in terms of the integral of the squared distances between all the

[1] Hu moment invariants were originally designed for single-component shapes.

pairs of the shape points. Such a new established relation leads to the definitions of the new analogues of the first Hu moment invariant, this time defined for multi-component shapes. These definitions exclude a 'special' role of the component centroids (see (5) and (6)), and give a more important role to the mutual positions between multi-shape components than in the case of invariants derived in [41]. The disconnectedness measure is also introduced and analyzed in Section 3. Section 4 provides a number of experiments, including synthetic ones and also experiments on applications performed by others in the literature. Concluding remarks are in the last section.

2. Preliminaries

Here we define the basic terms and introduce the notation used in this paper. Shape is one of the basic object properties (like color or texture, for example). As such, shape does not need a formal definition. Shape is represented by a planar region, usually displayed as a binary image. A multi-component shape $S = S_1 \cup S_2 \cup \ldots \cup S_n$, having components $S_1,\ S_2,\ \ldots,$ and S_n, is represented by n regions, corresponding to its components.

Note that the regions representing a component S_i do not need to be connected, in a topological sense. Actually, a multi-component shape $S = S_1 \cup S_2 \cup \ldots \cup S_n$, consisting of n components, can be formally defined by a mapping $F((x,y))$ of a planar region, representing S, onto a set of integers $\{1,2,\ldots,n\}$. All the points (x,y) with the same assigned value $F((x,y))$, from $\{1,2,\ldots,n\}$, belong to the same component. Formally, the component $S_i,\ i = 1,\ldots,n$ is defined as follows

$$S_i \ = \ \{(x,y) \mid F((x,y)) = i\} \ = \ F^{-1}(i), \ \text{ for all } i = 1,2,\ldots,n.$$

There is no formal restriction on how a given object, presented on an image, can be decomposed and presented as a multi-component shape. From a practical view-point such a decomposition should be meaningful in order to be beneficial for the desired application.

Two shapes will be considered to be equal if their set difference has area equal to zero – e.g. the open ellipse $\{(x,y) \mid x^2 + 2 \cdot y^2 < 1\}$ and the closed one $\{(x,y) \mid x^2 + 2 \cdot y^2 \leq 1\}$ are considered to be equal in shape. Obviously, this is not a restriction once dealing with images of real objects.

The *geometric moment*, or simply *moment*, $M_{p,q}(S)$ of a given planar shape S is defined as

$$M_{p,q}(S) = \iint_S x^p y^q dx\, dy. \tag{1}$$

The moment $M_{p,q}(S)$ has the *order* equal to $p+q$. Obviously, the zeroth order moment, $M_{0,0}(S)$, equals the area of S, while the first order moments $M_{1,0}(S)$ and $M_{0,1}(S)$ are used to define the *shape centroid*, denoted as $(x_c(S),\ y_c(S))$ and formally defined as

$$(x_c(S),\ y_c(S)) \ = \ \left(\frac{M_{1,0}(S)}{M_{0,0}(S)},\ \frac{M_{0,1}(S)}{M_{0,0}(S)} \right). \tag{2}$$

Moments $M_{p,q}(S)$ are not translation invariant, i.e. they change if the shape S is translated for a given vector. Since translation invariance is a necessary property in shape based image processing and computer vision tasks (shape does not change under translation), so called the *central moments*, $\overline{M}_{p,q}(S)$ have been used. They are defined as

$$\begin{aligned}\overline{M}_{p,q}(S) &= \iint\limits_S (x - x_c(S))^p\,(y - y_c(S))^q\,dx\,dy \\ &= \iint\limits_S \left(x - \frac{M_{1,0}(S)}{M_{0,0}(S)}\right)^p \left(y - \frac{M_{0,1}(S)}{M_{0,0}(S)}\right)^q dx\,dy. \end{aligned} \tag{3}$$

Central moments $\overline{M}_{p,q}(S)$ have translation invariance by definition.

Scaling invariance is also a requirement for the quantities used in shape based tasks. This is because shape does not change under scaling transformations. Central moments $\overline{M}_{p,q}(S)$, as given in (3), are not scaling invariant but they can be easily modified to provide the scaling invariance property. Indeed, if the central moments $\overline{M}_{p,q}(S)$ are multiplied with a properly chosen constant we obtain scaled *normalized moments* $\mu_{p,q}(S)$, defined as,

$$\mu_{p,q}(S) = \frac{1}{M_{0,0}(S)^{(p+q+2)/2}} \cdot \overline{M}_{p,q}(S) \tag{4}$$

which are both translation and scaling invariance.

Another invariance property is also a requirement if shape based tools are designed. This property is invariance under shape rotations. In his seminal work [19], Hu introduced seven quantities which are rotational invariants. Hu used algebraic reasoning, but later on Xu and Li [35] showed that Hu invariants are actually geometric invariants, and can be derived by considering certain geometric primitives defined by the shape points. In this work we are interested in the geometric interpretation [35] of the first Hu moment invariant.

The first Hu moment invariant [19]

$$\begin{aligned}\mathcal{H}(S) &= \mu_{2,0}(S) + \mu_{0,2}(S) \\ &= \frac{1}{M_{0,0}(S)^2} \cdot \left(\overline{M}_{2,0}(S) + \overline{M}_{0,2}(S)\right)\end{aligned} \tag{5}$$

can be derived [35] by considering the integral of the squared distances of all the shape points to the shape centroid. This integral can be expressed as $\overline{M}_{2,0}(S) + \overline{M}_{0,2}(S)$, as shown by the equality in (6). We will also later need the expression in (7).

$$\begin{aligned}\overline{M}_{2,0}(S) + \overline{M}_{0,2}(S) &= \iint\limits_S \left(x - \frac{M_{1,0}(S)}{M_{0,0}(S)}\right)^2 dx\,dy + \iint\limits_S \left(y - \frac{M_{0,1}(S)}{M_{0,0}(S)}\right)^2 dx\,dy \\ &= \iint\limits_S \left(\left(x - \frac{M_{1,0}(S)}{M_{0,0}(S)}\right)^2 + \left(y - \frac{M_{0,1}(S)}{M_{0,0}(S)}\right)^2\right) dx\,dy \qquad (6) \\ &= M_{2,0}(S) + M_{0,2}(S) - \frac{M_{1,0}(S)^2}{M_{0,0}(S)} - \frac{M_{0,1}(S)^2}{M_{0,0}(S)}. \qquad (7)\end{aligned}$$

Thus, the observations above, together with the equality in (5), give that the first Hu moment invariant $\mathcal{H}(S)$ equals the normalized[2] integral of the squared distances of all the shape points to the shape centroid.

[2]The normalization has been made taking into account the shape area and the requirement for scaling invariance.

Such an interpretation of the first Hu moment invariant has been used in [41] to define three moment invariants for multi-component shapes. Basically, such invariants are computed based on the different averaging of the invariants of the shape components. In this paper we will give another interpretation of $\mathcal{H}(S)$ which will be the basis for the developments in the rest of the paper.

3. Disconnectedness Measure for Multi-component Shapes

As it has been mentioned, in this section we give another interpretation of the first Hu moment invariant and will exploit such an interpretation to derive a new measure for multi-component shapes. First, we consider the integral $\mathcal{T}(S)$ of the squared distances between all the pairs of the shape points.

$$\begin{aligned}\mathcal{T}(S) &= \frac{1}{2}\cdot \iint\limits_{(x,y)\in S}\ \iint\limits_{(u,w)\in S} \left((x-u)^2+(y-w)^2\right) dx\,dy\,du\,dv \\ &= \frac{1}{2}\cdot \iint\limits_{(x,y)\in S}\ \iint\limits_{(u,w)\in S} \left(x^2+u^2+y^2+w^2-2xu-2yw\right)\, dx\,dy\,du\,dv \\ &= M_{0,0}(S)\cdot\left(M_{2,0}(S)+M_{0,2}(S)\right)-\left(M_{1,0}(S)^2+M_{0,1}(S)^2\right) \end{aligned} \tag{8}$$

Note. *The last equality comes from*

$$\iint\limits_{(x,y)\in S}\ \iint\limits_{(u,w)\in S} x^p y^q u^r w^s dx\,dy\,du\,dv \quad = \quad M_{p,q}(S)\cdot M_{r,s}(S).$$

So, (7) and (8) give

$$\mathcal{T}(S) \;=\; M_{0,0}(S)\cdot\left(\overline{M}_{2,0}(S)+\overline{M}_{0,2}(S)\right) \tag{9}$$

or, equivalently

$$\frac{1}{M_{0,0}(S)^3}\cdot\mathcal{T}(S) \quad = \quad \frac{1}{M_{0,0}(S)^2}\cdot\left(\overline{M}_{2,0}(S)+\overline{M}_{0,2}(S)\right) \;=\; \mathcal{H}(S). \tag{10}$$

In other words, the first Hu moment invariant can be expressed in terms of the normalized value of the squared distances between all the pairs of points which belong to the considered shape.

If we progress with similar reasoning we deduce that for a given 2-component shape $S=S_1\cup S_2$, the following quantity

$$\begin{aligned}&\mathcal{T}(S_1\cup S_2)-\mathcal{T}(S_1)-\mathcal{T}(S_2) \;= \\ &\quad = M_{0,0}(S_1\cup S_2)^3\cdot\mathcal{H}(S_1\cup S_2)-M_{0,0}(S_1)^3\cdot\mathcal{H}(S_1)\;-\;M_{0,0}(S_2)^3\cdot\mathcal{H}(S_2)\end{aligned} \tag{11}$$

equals the normalized integral squared distances between points belonging to different components of $S=S_1\cup S_2$ (the equality in (10) has been used).

The formula in (11) extends easily to n-component shapes $S = S_1 \cup S_2 \cup \ldots \cup S_n$, as follows,

$$\mathcal{T}(S_1 \cup S_2 \cup \ldots \cup S_n) - \sum_{i=1}^{n} \mathcal{T}(S_i) \ =$$

$$= \ M_{0,0}(S_1 \cup S_2 \cup \ldots \cup S_n)^3 \cdot \mathcal{H}(S_1 \cup S_2 \cup \ldots \cup S_n) \ - \ \sum_{i=1}^{n} M_{0,0}(S_i)^3 \cdot \mathcal{H}(S_i) \qquad (12)$$

and the quantity $\mathcal{T}(S) - \sum_{i=1}^{n} \mathcal{T}(S_i)$ in (12) equals the normalized integral of the squared distances between all the pair of points in $S_1 \cup S_2 \cup \ldots \cup S_n$, which do not belong to the same component. Such a quantity may be expected to be an efficient and natural characteristic of multi-component shapes, since it expresses somehow how much the set $S_1 \cup S_2 \cup \ldots \cup S_n$ is disconnected. Indeed, more shape components and longer mutual distances between them would imply a larger value of $\mathcal{T}(S) - \sum_{i=1}^{n} \mathcal{T}(S_i)$.

The quantity $\mathcal{T}(S) - \sum_{i=1}^{n} \mathcal{T}(S_i)$ is translation and rotation invariant. This is because it can be expressed (see (12)) in terms of the area and the first Hu moment invariants corresponding to the n-component shape $S_1 \cup S_2 \cup \ldots \cup S_n$ and its components S_i, $i = 1, 2, \ldots, n$, which are such invariants. In order to have the scaling property satisfied, the quantity $\mathcal{T}(S) - \sum_{i=1}^{n} \mathcal{T}(S_i)$ should be normalized. This can be done in several ways. Herein the normalization is done by using the factor $M_{0,0}(S_1 \cup S_2 \cup \ldots \cup S_n)^{-3}$. Such a normalized value obtained is named a *multi-component shape disconnectedness measure*, and will be denoted as $\mathcal{D}(S_1 \cup S_2 \cup \ldots \cup S_n)$, i.e. $\mathcal{D}(S)$. The formal definition for $\mathcal{D}(S_1 \cup S_2 \cup \ldots \cup S_n)$ is as follows.

Definition 1. *Given a multi-component shape $S = S_1 \cup S_2 \cup \ldots \cup S_n$ the disconnectedness measure $\mathcal{D}(S)$ of the n-component shape S is defined as*

$$\mathcal{D}(S) \ = \ \frac{1}{M_{0,0}(S_1 \cup S_2 \cup \ldots \cup S_n)^3} \cdot \left(\mathcal{T}(S_1 \cup S_2 \cup \ldots \cup S_n) - \sum_{i=1}^{n} \mathcal{T}(S_i) \right) \qquad (13)$$

or equivalently

$$\mathcal{D}(S) \ = \ \mathcal{H}(S_1 \cup S_2 \cup \ldots \cup S_n) \ - \ \frac{1}{M_{0,0}(S_1 \cup S_2 \cup \ldots \cup S_n)^3} \cdot \sum_{i=1}^{n} M_{0,0}(S_i)^3 \cdot \mathcal{H}(S_i). \qquad (14)$$

Several properties of the new multi-component shape measure $\mathcal{D}(S)$ are listed in the next theorem.

Theorem 1. *Given a multi-component shape $S = S_1 \cup S_2 \cup \ldots \cup S_n$ the following statements are true:*

(a) $\mathcal{D}(S)$ is invariant with respect to translation, rotation, and scaling transformations;

(b) If $n = 1$ (i.e. if $S = S_1$), meaning that S consists of a single component, then $\mathcal{D}(S) = 0$;

(c) $\mathcal{D}(S)$ ranges over the interval $[0, \infty)$;

(d) If n varies (i.e. the shape S is partitioned into various numbers of components), the following estimate

$$\mathcal{D}(S) < \mathcal{H}(S) \qquad (15)$$

is true for all n and S;

(e) the upper bound $\mathcal{H}(S)$ in (15) is the best possible.

Proof. *Each statement from the theorem is proven/discussed separately.*

(a) The translation and rotation invariance of $\mathcal{D}(S)$ comes from (14) and the fact that both the first Hu moment invariant and the shape area are such invariants. The scaling invariance, i.e. the equality[3]

$$\mathcal{D}(S) \;=\; \mathcal{D}(r\cdot S)$$

for all shapes and all $r>0$, comes from the expression in (14) and the facts:
– $\mathcal{H}(S)$ is scaling invariant, and
– $M_{0,0}(r\cdot S) \;=\; r^2\cdot M_{0,0}(S)$;

(b) This follows from (14), by setting $n=1$;

(c) This statement can be proven by setting $n=1$ and the properties of $\mathcal{H}(S)$ (see the observations in [28], for example);

(d) The estimate in (15) follows from (14) and $\mathcal{H}(S_i)>0$, for all $i=1,2,\ldots,n$;

(e) Let S be the square with vertices $(0,0)$, $(m,0)$, (m,m), and $(0,m)$ partitioned onto $n=m^2$ unit area squares, determined by the vertical lines $x=0$, $x=1,\ldots$ $x=m$ and the horizontal lines $y=0$, $y=1,\ldots$ $y=m$. Thus, S can be seen as an m^2-component shape:

$$S=S_1\cup S_2\cup\ldots\cup S_n$$

having area $n=m^2$ and each of its components S_i $(i=1,2,\ldots,n=m^2)$ has area equal to 1. Since all the squares have the same first Hu moment invariant (equal to $1/6$, see (5)), we have

$$\mathcal{H}(S)=\mathcal{H}(S_1)=\mathcal{H}(S_2)=\ldots=\mathcal{H}(S_n)=\frac{1}{6}. \tag{16}$$

Further, (14) and (16) give

$$|\mathcal{D}(S)\;-\;\mathcal{H}(S)| \;=\; \frac{1}{M_{0,0}(S)^3}\cdot\sum_{i=1}^{n} M_{0,0}(S)^3\cdot\mathcal{H}(S_i) \;=\; \frac{1}{n^3}\cdot n\cdot\frac{1}{6}=\frac{1}{6\cdot m^4}. \tag{17}$$

This establishes the proof, since $\lim_{m\to\infty}|\mathcal{D}(S)\;-\;\mathcal{H}(S)|=\lim_{m\to\infty}\frac{1}{6\cdot m^4}=0.$ □

4. Experimental validation

In this section we provide a number of experiments. Synthetic experiments are in the first subsection; they are given in order to support a better understanding of the disconnectedness measure $\mathcal{D}(S)$ that has been introduced in this paper. The experiments in the second subsection illustrate the effectiveness of $\mathcal{D}(S)$ in various tasks, performed on existing image data and in applications reported by others in the literature.

4.1. Experimental Illustrations of $\mathcal{D}(S)$ Behavior

As it has been mentioned, in this section, we provide several experiments to illustrate the behavior of the novel multi-component shape measure $\mathcal{D}(S)$. These experiments are designed to illustrate and validate the theoretical considerations and properties of the new measure that have been proven in the previous section.

[3] $r\cdot S=\{(r\cdot x, r\cdot y)\mid (x,y)\in S\}$ equals the dilation of the shape S for a coefficient $r>0$.

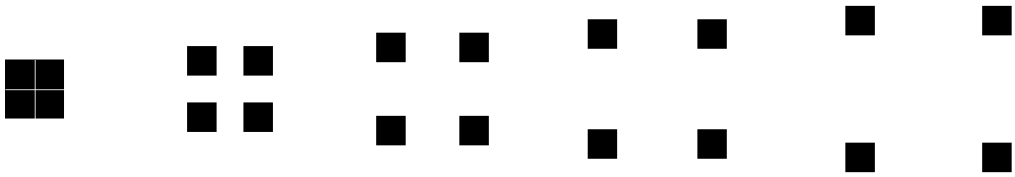

(a) 0.1562 (b) 0.4868 (c) 1.0240 (d) 1.7678 (e) 2.7182

Figure 3: 4-component shapes and their assigned $\mathcal{D}(S)$ values (given below the shape)

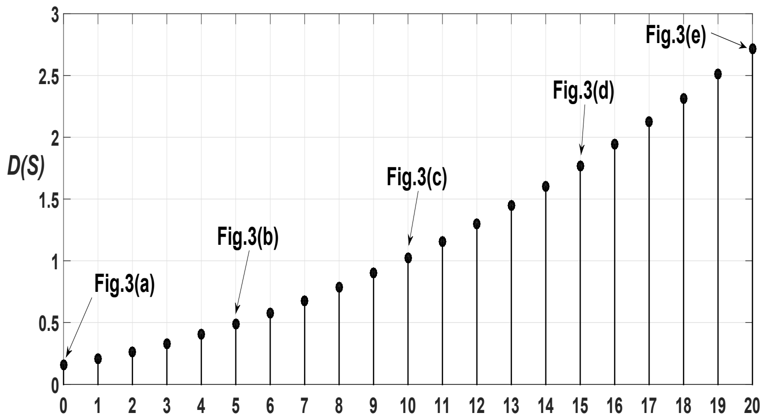

Figure 4: Plot of computed $\mathcal{D}(S)$ values for 4-component shapes, consisting of 4 identical squares, as given in Fig. 3.

First experiment. In order to illustrate how the measure $\mathcal{D}(S)$ depends on the distances between the components, we consider multi-component shapes, consisting of 4 identical squares. The 4-component shapes considered differ by the distance between the shape components (i.e. the distance between squares). Several examples of such 4-component shapes, are given in Fig. 3, together with their computed values of $\mathcal{D}(S)$. As expected, as the distance between the components (squares) increases then the computed disconnectedness increases too. The largest $\mathcal{D}(S)$ value for the five 4-component shapes presented in Fig. 3 is 2.7182. Of course, this is not the upper bound for the computed $\mathcal{D}(S)$ values of such shapes. Actually, $\mathcal{D}(S)$ can be arbitrarily large for a sufficiently large distance between the shape components. This is in accordance with formula (14), since all four squares (shape components) have the same first Hu moment invariant, while the first Hu moment invariant of the 4-component shape considered increases unboundedly, as the distance between the shape components increases too (which follows from the first Hu moment interpretation given). A plot of $\mathcal{D}(S)$ values for 21 values of increasing distances between the shape components (squares) is given in Fig. 4. The plot starts with $\mathcal{D}(S)$ value $\frac{5}{32} \approx 0.1562$ for zero distance between the shape components (the shape in Fig. 3(a); white lines between the squares are only indicative, i.e. they have the width equal to 0), and increases to the largest computed $\mathcal{D}(S)$ value 2.7182, corresponding to the shape in Fig. 3(e), that has the largest distance between the components, among the shapes presented.

Second experiment. In this experiment we illustrate how the disconnectedness measure $\mathcal{D}(S)$ behaves as the shape of the components and their number change. In the first row in Fig. 5, a square is

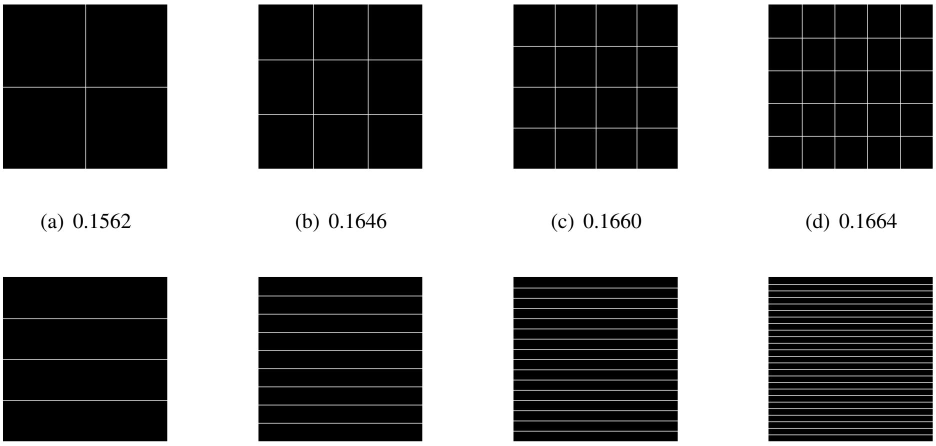

(a) 0.1562 (b) 0.1646 (c) 0.1660 (d) 0.1664

(e) 0.1445 (f) 0.1573 (g) 0.1614 (h) 0.1633

Figure 5: Multi-component shapes, consisting of 4, 9, 16 and 25 identical squares (first row) and 4, 9, 16 and 25 identical rectangles (second row). $\mathcal{D}(S)$ values are below the shape related.

partitioned onto 4, 9, 16 and 25 squares. In the second row, the same square is partitioned onto 4, 9, 16 and 25 identical rectangles. In both the set of partitions presented in the first row and the set of partitions presented in the second row, the computed $\mathcal{D}(S)$ values increase consistently with the number of the components. The values of $\mathcal{D}(S)$ for the 4-component shape in the first row and 4-component shape in the second row (0.1562 and 0.1445, respectively) differ because the disconnectedness value depends on the shape of the components, and not only on their number. The same reasoning applies to the shapes in the second, third, and fourth columns.

Third experiment. In this experiment we illustrate how the disconnectedness measure $\mathcal{D}(S)$ of a multi-component shape depends on the mutual positions of the shape components, i.e. it is dependent on the shape as whole. To illustrate this, three 4-component shapes, consisting of 4 identical discs arranged in different ways, are given in Fig. 6, together with their assigned $\mathcal{D}(S)$ values. The computed values of $\mathcal{D}(S)$ change as the overall structure of the 4-component shape changes. The obtained results are in accordance with our expectations, since the most disconnected shape (among the 4-component shapes displayed) is the shape on the left ($\mathcal{D}(S) = 0.6460$), while the most connected one is the shape on the right ($\mathcal{D}(S) = 0.2763$). The obtained results are also consistent with the theoretical observations. Indeed, in accordance with formula in (14), the change in the arrangement of the shape components only leads to the change in the value of the first Hu moment invariant $\mathcal{H}(S)$ of the whole shape. Since $\mathcal{H}(S)$ can be expressed in terms of the integral of the squared distances between all pairs of the points of S, as it has been shown in this paper earlier, the ranking among the shapes presented in Fig. 6 is as expected.

4.2. Validation of $\mathcal{D}(S)$ in Different Applications

In this subsection we show that the new multi-component shape measure is a generic image analysis tool that can be used efficiently for a spectrum of applications, which is why we provide a number of essentially different experiments. The experimental procedures used are relatively simple. This has been done in order to point out that the quality of the results is obtained by involving the new measure $\mathcal{D}(S)$, rather than by employing additional existing techniques that are known to improve the performance of image based tasks. For example, the classification experiments provided below, involve a small number

(a) 0.6460 (b) 0.4612 (c) 0.2763

Figure 6: Three 4-component shapes are presented, each consisting of four identical discs arranged in different ways. Computed $\mathcal{D}(S)$ values are given below each corresponding shape. The obtained ranking fits well with our perception of how the disconnectedness measure should act. In accordance with the measure $\mathcal{D}(S)$, the 4-component shape on the left is the most disconnected one (the measured $\mathcal{D}(S)$ is 0.6460), while among the presented shapes the 4-connected shape on the right is most connected one ($\mathcal{D}(S) = 0.2763$).

of shape measures and low dimensionality feature vector spaces. Indeed, in the last experiment a single feature has been used, whereas the results from [42] were obtained by using feature vectors of more than 150 dimensions.

To demonstrate the generality of the new measure and show situations in which it can be applied, the following have been done as well:

– Different kinds of data sets have been used in the experiments below. These include black and white images, color images, video sequences, and texture images.

– Various ways in which the disconnectedness measure can be applied to image data are shown. More precisely, the following are applied:

1. Given a binary image containing foreground objects, connected component analysis is performed, and the disconnectedness measure is applied to the set of connected components in the image.
2. The above approach can be applied locally, within all w_i $n \times n$ windows that contain foreground pixels, generating a set of disconnectedness values $\mathcal{D}^{w_i}(S)$. The final measure is the mean of $\mathcal{D}^{w_i}(S)$.
3. Instead of a set of components contained within an image, a set of images can be processed, treating all the foreground pixels in an image as a single component. In this approach we do not require components to be connected. Examples of such a multiple image set could be binary images from a time series (e.g. video), or else multiple binary image bands (e.g. a color image).
4. A gray level image can be thresholded at t levels to produce $t+1$ binary images, each of which are treated as a single component. Again, components need not be connected.
5. Finally, the above approach (item 4) can be applied locally, to generate a feature map of local disconnectedness values.

Fourth experiment. This experiment uses data from Yang *et al.* [43], who quantified the fabric anisotropy of granular soil in order to investigate its response under applied loading. 29 samples of Toyoura sand (see Fig. 7 for examples) were prepared using two different methods: 1/ moist tamping (MT) in which sand with 5% water content is laid down in layers and each layer is compacted, and 2/ dry deposition (DD) in which oven dried sand is poured using a funnel. Yang *et al.* [43] differentiated between the two preparation methods by characterizing the intensity of anisotropy of the preferred particle orientation using a measure (denoted Δ) related to the circular variance of the directions of the components.

We have applied our proposed measure of disconnectedness (following method 1, listed at the beginning of this subsection) to the soil samples in order to differentiate between the two preparation methods. Nearest neighbour classification with leave-one-out validation was applied, and the results in Table 1 show that $\mathcal{D}(S)$ provides substantially better accuracy than the anisotropy measure Δ. The first Hu moment invariant $\mathcal{H}(S)$ yields the same accuracy as $\mathcal{D}(S)$. In addition, the local version of the measure

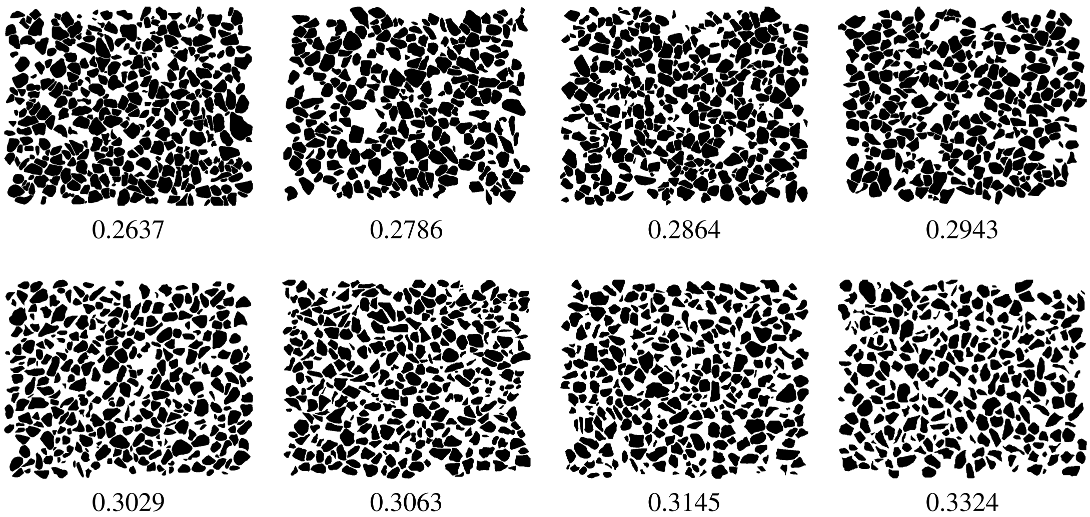

Figure 7: Examples of boundaries of SEM images of Toyoura sand (Japanese standard sand) prepared using two methods: moist tamping (first row), dry deposition (second row). $\mathcal{D}^{100}(S)$ values are shown below each example.

(method 2 in Section 4.2) was used, with 100×100 local windows. Table 1 shows that $\mathcal{D}^{100}(S)$ outperforms both $\mathcal{D}(S)$ and $\mathcal{H}(S)$. For comparison, the first Hu moment invariant was also computed as the average of the local values, but its performed dropped compared to its global version.

Table 1: Results for leave one out classification of SEM images of Toyoura sand.

Method	Δ	$\mathcal{D}(S)$	$\mathcal{H}(S)$	$\mathcal{D}^{100}(S)$	$\mathcal{H}^{100}(S)$
Accuracy	62.07	89.66	89.66	93.10	82.76

Fifth experiment. This experiment uses a subset of 524 color galaxy images from Galaxy Zoo [44] (see Fig. 8) that were selected[4] by Shamir [45] to demonstrate machine learning based classification into three classes: spiral, elliptical and edge-on galaxies. His approach uses a measure of spirality, which requires finding the foreground object by applying Otsu's thresholding algorithm [46], followed by generating a radial intensity plot from the estimated center of the galaxy, and then computing the slopes of the peaks detected in this plot. The images were manually classified by Shamir to provide a ground truth, although he notes that there are many in-between cases, and so the ground truth is not totally reliable. He achieves a classification accuracy of 88.76%.

Using disconnectedness along with a variety of other standard shape measures we achieve almost the same result: a leave-one-out accuracy of 88.55%. Specifically, a minimum Mahalanobis distance classifier was applied to the the first and fourth affine invariant moments [47], convex hull perimeter based convexity (denoted as $\mathcal{C}_3$ in [26]), ellipticity (denoted E_E in [31]), and compactness (i.e. the ratio of the squar-ed perimeter and area) as well as three versions of disconnectedness:

- Otsu's thresholding was applied to the three channels of the color image, and the three binary images specified the three components (method 3, listed at the beginning of this subsection).

[4] Although Shamir [45] states the subset contains 525 images, the zip file that he provides only contains 524 images.

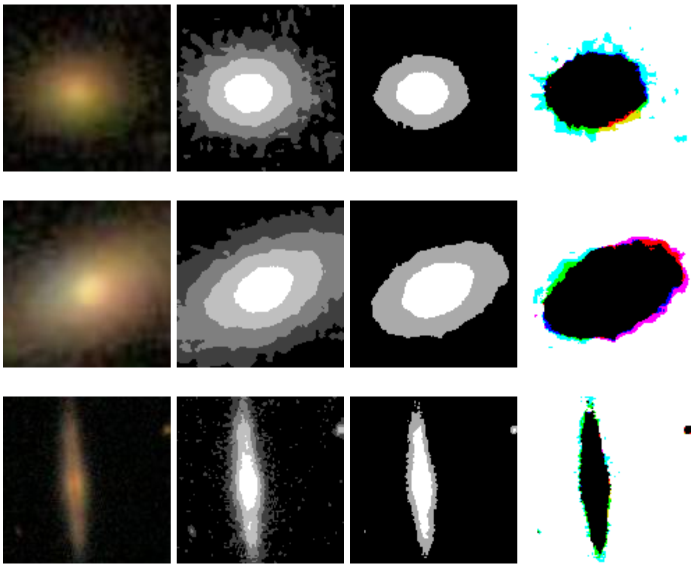

Figure 8: Examples of the three classes of galaxy images selected from Galaxy Zoo. Rows (top to bottom): elliptical, spiral, edge-on. Columns (left to right): original image; thresholded into five components; thresholded into three components with the bottom two components merged; three color channels thresholded into two components (visualised as a color image).

- Multi-class Otsu thresholding was applied to a grayscale version of the image to determine four thresholds, which segmented the images into five (potentially non-connected) components. The component arising from the darkest pixels tends to correspond to background, and so only the other four components were used (method 4, listed at the beginning of this subsection).
- The same as the above was applied, but using three thresholds, and keeping only the upper two components.

We also note that when performing classification using a single feature that disconnectedness was relatively effective. Leave-one-out accuracy is 75.38% and 70.99% for the two disconnectedness measures used above, while the best moment invariant was the first Hu moment invariant applied to the Otsu thresholded image (63.36%). The remaining Hu moments applied to the binary or grayscale image produced classification accuracies of 60% or less.

Sixth experiment. This experiment uses the silhouettes from video sequences analysed by [48] *et al.* to perform human action recognition. There are 90 video sequences of lengths between 28 and 146 frames, showing nine different people, each performing 10 actions such as run, walk, skip, etc. Gorelick *et al.* achieved 100% classification accuracy by using the Poisson equation to extract space-time features such as local space-time saliency, action dynamics, shape structure, and orientation. Here we show a simpler approach, using standard global 2D shape features plus our disconnectedness measure, to achieve 80% classification accuracy, in order to show that such simple features can still be reasonably effective. Disconnectedness is computed over the set of silhouettes for each sequence (method 3 in Section 4.2). Each sequence was processed to produce two composite images that capture some elements of the dynamics of the sequence, see Fig. 9 for examples.

- At each pixel the mean intensity over the complete sequence of silhouettes was computed, and the result was binarised by applying Otsu's thresholding algorithm. Finally, the single largest

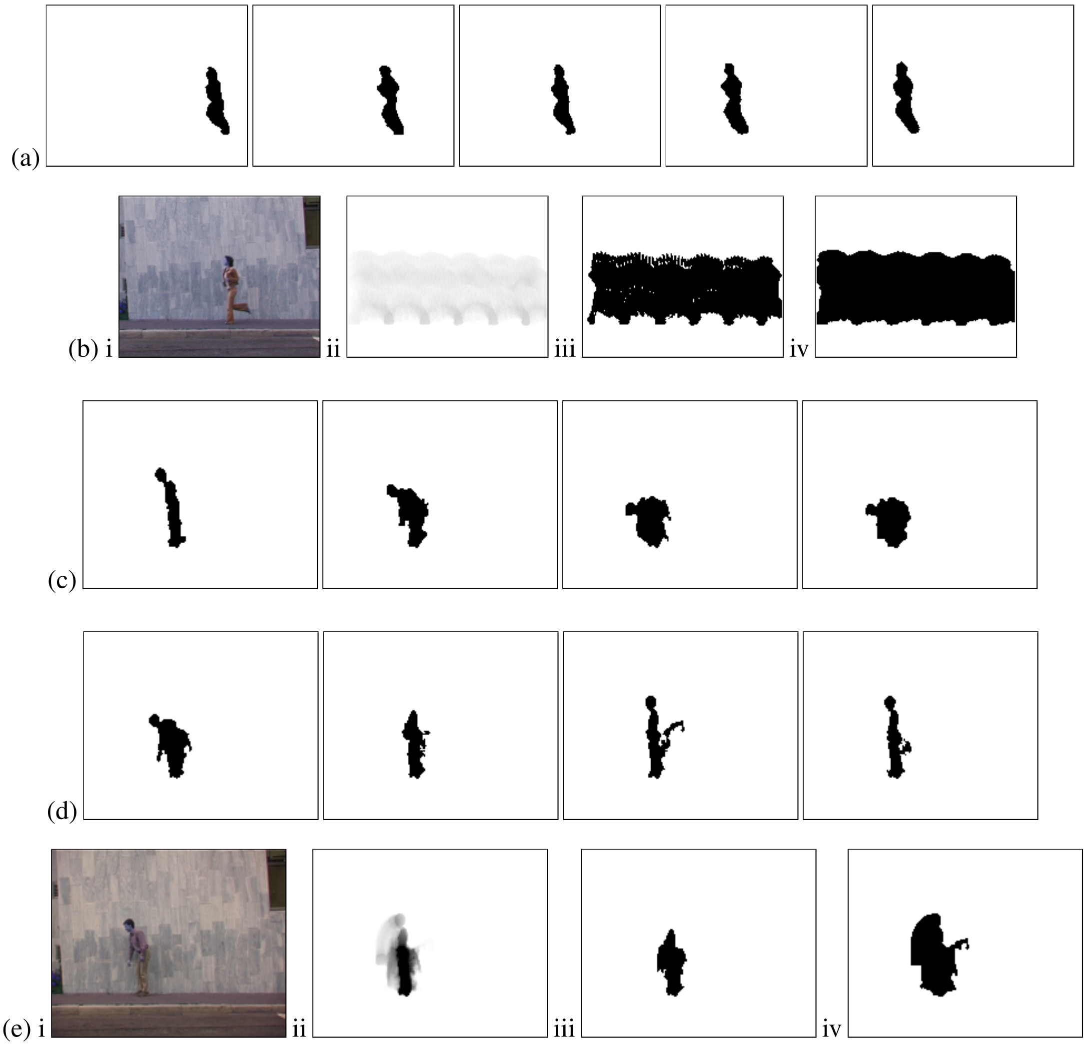

Figure 9: Regions extracted and analysed from video sequences containing human action. Example regions for two sequences are shown in (a) and (c)-(d). The contents of each sequence are summarised by single regions as shown in (b) and (e). (a) silhouettes extracted from five sample frames of a sequence containing a running person; (b) i: sample frame from the middle of the running video; ii: mean pixel intensities are computed over the sequence containing 56 images of running silhouettes; iii: image of mean pixel intensities after thresholding; iv: black pixels indicate those pixels which appear as foreground pixels in any of the 56 frames in the running sequence, (c) & (d) silhouettes extracted from eight sample frames of a sequence containing a bending person; (e) i: sample frame from the middle of the bending video; ii: mean pixel intensities are computed over the sequence containing 85 images of bending silhouettes; iii: image of mean pixel intensities after thresholding; iv: black pixels indicate those pixels which appear as foreground pixels in any of the 85 frames in the bending sequence.

connected component was retained. The shape was described by ellipticity [33] and triangularity (method T_P in [31]).

- A mask image was created which identified which pixels contained a foreground value within the complete sequence of silhouettes. All such masks were found to contain only a single connected component. This shape was then described by the third and fifth Hu moment invariants and by the second affine moment invariant.

The accuracy of classifying the 10 actions was 80%. When the disconnectedness measure was removed accuracy dropped to 61.11%.

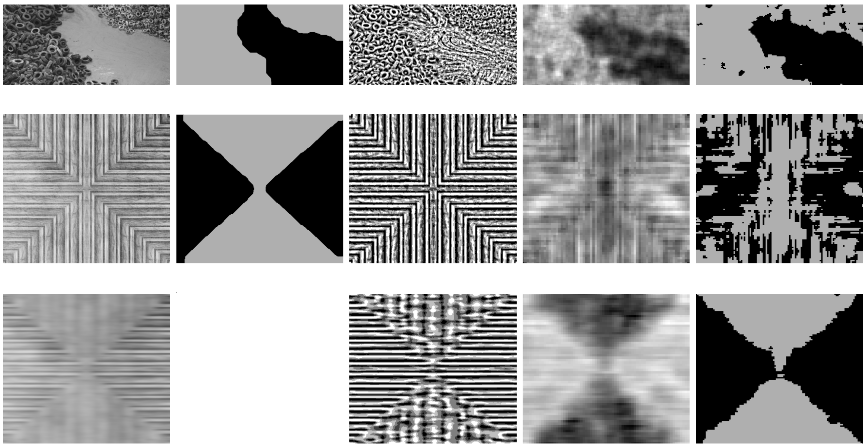

Figure 10: Application of the disconnectedness measure for texture segmentation. Columns (left to right) for rows 1–2: source image, segmentation result from [42], pre-processed source image, feature map of local disconnectedness values, segmentation result using disconnectedness. Row 3: processing of the 2nd source image which has been filtered by anisotropic blurring. Note that no result is shown for [42] for this filtered version of the image.

Seventh experiment. This experiment provides some preliminary results of local disconnectedness values to perform unsupervised texture segmentation. Two images from figure 1 in [42] are shown in figure 10. First we perform pre-processing: adaptive histogram equalization (using a window size of 8×8) is applied to normalise local contrast; the effect of noise is reduced by applying a small amount of Gaussian blurring ($\sigma = 1$); and finally the image is simplified by quantizing the number of intensities using multi-class Otsu thresholding to produce four (potentially non-connected) components. The pre-processed images and their disconnectedness feature maps (calculated using 40×40 windows) are shown in columns 3 and 4 of figure 10. For simplicity we assume that the number of texture classes is known, and apply binary Otsu thresholding to the feature maps to produce the image segmentation shown in the final column of figure 10. Compared to [42] local disconnectedness has performed well on the first image. This is despite the fact that our approach has no spatial model and uses a single feature, whereas [42] uses a Potts model and feature vectors of more than 150 dimensions.

Since the disconnectedness measure does not incorporate any orientation specific information, its use for segmentation of the second image is ineffective, as the two patterns are the same, modulo orientation. However, an orientation aware version of the disconnectedness measure can be produced by pre-processing the image to highlight structures at specific orientations. This is demonstrated in the bottom row, which shows the image after anisotropic Gaussian blur; we use the fast method by [49], which is steered in the orientation of one of the patterns ($\sigma = \{1,8\}, \theta = 0°$). The resulting texture segmentation now closely matches the results from [42].

4.3. Sensitivity of $\mathcal{D}(S)$ to Noise

When applying the $\mathcal{D}(S)$ measure to a set of regions extracted from image data (for example), the results will naturally be dependent on the grouping of the pixels to form regions. In turn, this will depend not only on the underlying scene captured in the image, but also on the segmentation algorithm, noise, illumination, and so on. In this subsection we perform an experiment to illustrate the performance of the new multi-component shape measure when noise is added to the data already presented in the fourth experiment on classifying SEM images of Toyoura sand.

Eighth experiment.

For each image, a 4×4 block of salt and pepper noise was added at each location with a specified probability, and then the noisy images were classified as previously described in the fourth experiment. This process was repeated ten times, and the classification results are shown in Fig. 11. It can be seen that, even for large amounts of noise, the $\mathcal{D}(S)$ measure enabled effective classification for this application. Surprisingly, small amounts of noise improved the classification accuracy. This can be explained as a consequence that the added noise causes some close regions to become connected. Therefore, if one of the types of sand has regions that are closer together than the other type of sand, then this effect will affect it more strongly compared to the other type of sand, leading to the disconnected measure becoming more differentiated between the two types of sand, thereby improving classification. Of course, if the noise level becomes too high, then not only do both types of sand become affected in a similar way, but the signal becomes swamped by the noise, resulting in low classification accuracy.

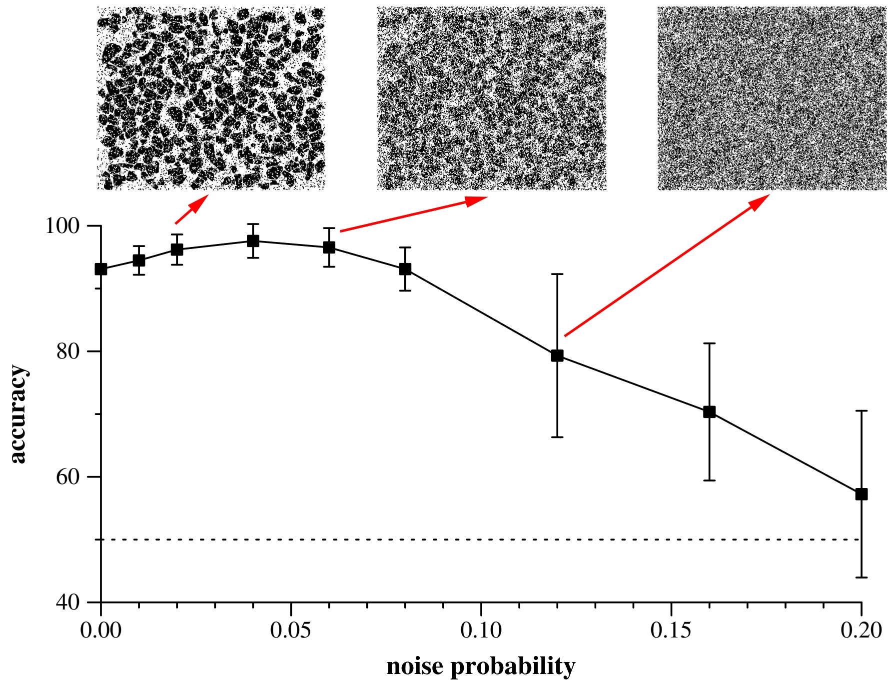

Figure 11: Classification accuracies (mean and one standard deviation error bars) of SEM images of Toyoura sand with varying amounts of added salt and pepper noise. The dotted line shows the expected classification accuracy that would be achieved by random guessing. Examples of an image with different noise levels are shown.

5. Concluding Remarks

A new measure for multi-component shapes has been introduced. The measure is named the disconnectedness measure, and is denoted as $\mathcal{D}(S)$. This is the second known measure designed to evaluate numerically some intuitive shape properties related to the multi-component shapes. The first such measure was the anisotropy of multi-component shapes, introduced in [38]. The new measure $\mathcal{D}(S)$ aims to evaluate how much a given multi-component shape S is disconnected, where the word "disconnected" is taken in an informal, but intuitively clear, sense. For a single-component shape, $\mathcal{D}(S)$ takes the value zero, and this is the lowest possible value for $\mathcal{D}(S)$. There is no upper bound for $\mathcal{D}(S)$, i.e. $\mathcal{D}(S)$ can be arbitrary large for a suitable choice of S. The measure $\mathcal{D}(S)$ is invariant with respect to translation, rotation, and scaling transformations. $\mathcal{D}(S)$ depends on the number of components of S, on the overall shape of S, and on the shapes of the components of S. It also depends on the mutual positions of the components of S, as well as their relative sizes.

The measure $\mathcal{D}(S)$ is derived based on the new interpretation of the first Hu moment invariant, and can be expressed in terms of the first Hu moment invariant of the shape S and the first Hu moment invariants of the components of S. This implies that the computation of $\mathcal{D}(S)$ is fast and straightforward.

The new measure $\mathcal{D}(S)$ is a generic tool, not designed for a particular application. As such, it can be used for a wide spectrum of image processing based tasks. Several of them are provided in this paper, and aim to show the usability and effectiveness of $\mathcal{D}(S)$ in different situations. This is why we were focused on a number of experiments (different by their nature and data sets used), rather than on a particular task. First, we have used synthetic data (images) suitable for a better understanding of the behavior of the new measure. Those also validate the theoretical observations and proven statements about the properties of the new measure. After that we have employed the new measure in several well known tasks, based on different data sets consisting of different kind of images (black and white images, color images, video sequences, and texture images). A good performance in all of them has been obtained, even though we have used simple procedures and techniques, usually based on a few shape measures. This points out the importance and crucial role of the new measure in the tasks performed.

The future work on the multi-component shape based approach to object analysis tasks can be explored in several directions. Due to the novelty of the concept, the properties specifically related to multi-component shapes have been little studied. More of such properties should be recognized, and procedures for their numerical evaluation developed. So far, the anisotropy and disconnectedness measures are the only recognized and studied multi-component shape properties, but more are expected to be discovered. Note that there also exist methods for a formal extension of the existing measures designed for single-component shapes, that do not relate to specific shape properties. Several of them have already been employed and evaluated on a leaf classification problem [41]. The same paper uses a simple method to decompose a given shape onto an arbitrary number of components using different circles centred at the shape centroid. In the current paper further methods are used to represent real objects (presented as digital images) by their corresponding multi-component shapes. However, more methods that would suit specific applications need to be investigated.

Another specific problem, appearing when dealing with multi-component shapes, relates to the influence of the shape components' size on the numerical evaluation of shape properties. Such a problem does not exist if dealing with single component shapes, since the overall shape does not change under scaling transformations. The situation changes when working with multi-component shapes. For example, the extracted shape components might be of a different size, but still corresponding to equal sized objects. The difference could simply come from the fact that the observed objects are positioned differently with respect to the camera. Thus, the issue of appropriately weighting the influence of component size arises naturally in such situations. Such problems are just some of those that have already been seen as important ones. During the exploitation of the multi-component shape approach in different tasks, more problems are expected to arise.

Acknowledgements

This work is partially supported by the Ministry of Science of the Republic of Serbia.

References

[1] M. Breuß, A. Bruckstein, P. Maragos, S. Wuhrer, Perspectives in Shape Analysis, Springer, 2016.

[2] F. Cao, J.-L. Lisani, J.-M. Morel, P. Musé, F. Sur, A theory of shape identification, Springer, 2008.

[3] L. d. F. Costa, R. M. Cesar Jr, Shape classification and analysis: theory and practice, CRC Press, 2009.

[4] R. Davies, C. Taylor, et al., Statistical models of shape: Optimisation and evaluation, Springer Science & Business Media, 2008.

[5] S. Dickinson, Z. Pizlo, Shape perception in human and computer vision, Springer, 2015.

[6] I. L. Dryden, K. V. Mardia, Statistical Shape Analysis: With Applications in R, John Wiley & Sons, 2016.

[7] S. Li, J. M. R. Tavares, Shape Analysis in Medical Image Analysis, Vol. 14, Springer Science & Business Media, 2014.

[8] M. A. Aktaş, J. Žunić, A family of shape ellipticity measures for galaxy classification, SIAM Journal on Imaging Sciences 6 (2013) 765–781.

[9] T. Kitching, J. Rhodes, C. Heymans, R. Massey, Q. Liu, M. Cobzarenco, B. Cragin, A. Hassaine, D. Kirkby, E. J. Lok, et al., Image analysis for cosmology: Shape measurement challenge review & results from the mapping dark matter challenge, Astronomy and Computing 10 (2015) 9–21.

[10] M. Ruela, C. Barata, J. S. Marques, J. Rozeira, A system for the detection of melanomas in dermoscopy images using shape and symmetry features, Computer Methods in Biomechanics and Biomedical Engineering: Imaging & Visualization 5 (2017) 127–137.

[11] J. Russell, N. Hasler, R. Klette, B. Rosenhahn, Automatic track recognition of footprints for identifying cryptic species, Ecology 90 (2009) 2007–2013.

[12] A. A. Patil, K. Bhagat, Plant identification by leaf shape recognition: a review, International Journal of Engineering Trends and Technology 8 (35) (2016) 359–361.

[13] D. Jasani, P. Patel, S. Patel, B. Ahir, K. Patel, M. Dixit, Review of shape and texture feature extraction techniques for fruits, International Journal of Computer Science and Information Technologies 6 (6) (2015) 4851–4854.

[14] M. L. Merrill, Curvature-based method for the morphometric analysis of archaeological shapes, Mathematics and Archaeology (2015) 157.

[15] H. Li, F. Sun, L. Liu, L. Wang, A novel traffic sign detection method via color segmentation and robust shape matching, Neurocomputing 169 (Supplement C) (2015) 77 – 88.

[16] G. Bagheri, C. Bonadonna, I. Manzella, P. Vonlanthen, On the characterization of size and shape of irregular particles, Powder Technology 270 (2015) 141–153.

[17] L. Kopanja, D. Žunić, B. B. Lončar, G. Saso, M. M. Tadić, Quantifying shapes of nanoparticles using modified circularity and ellipticity measures, Measurement 92 (2016) 252–263.

[18] V. Nikolić, M. M. Tadić, M. Panjan, L. Kopanja, N. D. Cvjetičanin, V. V. Spasojević, Influence of annealing treatment on magnetic properties of Fe2O3/SiO2 and formation of epsilon-Fe2O3, Ceramics International 43 (2017) 3147–3155.

[19] M. K. Hu, Visual pattern recognition by moment invariants, IRE Transactions on Information Theory 8 (2) (1962) 179–187.

[20] S. Manay, D. Cremers, B. W. Hong, A. Yezzi, S. Soatto, Integral invariants for shape matching, IEEE Transactions on Pattern Analysis and Machine Intelligence 28 (2006) 1602–1618.

[21] Y. Mei, D. Androutsos, Robust affine invariant region-based shape descriptors: The ICA Zernike moment shape descriptor and the whitening Zernike moment shape descriptor, IEEE Signal Processing Letters 16 (2009) 877–880.

[22] B. Wang, Shape retrieval using combined Fourier features, Optics Communications 284 (2011) 3504–3508.

[23] T. Suk, J. Flusser, Affine moment invariants generated by graph method, Pattern Recognition 44 (9) (2011) 2047–2056.

[24] E. Rahtu, M. Salo, J. Heikkilä, A new convexity measure based on a probabilistic interpretation of images, IEEE Transactions on Pattern Analysis and Machine Intelligence 28 (9) (2006) 1501–1512.

[25] P. L. Rosin, C. L. Mumford, A symmetric convexity measure, Computer Vision and Image Understanding 103 (2006) 101–111.

[26] J. Žunić, P. L. Rosin, A new convexity measurement for polygons, IEEE Transactions on Pattern Analysis and Machine Intelligence 26 (7) (2004) 923–934.

[27] R. S. Montero, E. Bribiesca, State of the art of compactness and circularity measures, International Mathematical Forum 4 (27) (2009) 1305–1335.

[28] J. Žunić, K. Hirota, P. L. Rosin, A Hu invariant as a shape circularity measure, Pattern Recognition 43 (1) (2010) 47–57.

[29] P. L. Rosin, J. Žunić, Measuring squareness and orientation of shapes, Journal of Mathematical Imaging and Vision 39 (2011) 13–27.

[30] E. Grisan, M. Foracchia, A. Ruggeri, A novel method for the automatic grading of retinal vessel tortuosity, IEEE Transactions on Medical Images 27 (2008) 310–319.

[31] P. L. Rosin, Measuring shape: Ellipticity, rectangularity, and triangularity, Machine Vision and Applications 14 (3) (2003) 172–184.

[32] A. Q. Tool, A method for measuring ellipticity and the determination of optical constants of metals, Physical Review (Series I) 31 (1910) 1–25.

[33] D. Žunić, J. Žunić, Shape ellipticity based on the first Hu moment invariant, Information Processing Letters 113 (19) (2013) 807–810.

[34] J. Žunić, R. Kakarala, M. Ali Aktaş, Notes on shape based tools for treating the objects ellipticity issues, Pattern Recognition, accepted, DOI:10.1016/j.patcog.2017.04.009 69 (2017) 141–149.

[35] D. Xu, H. Li, Geometric moment invariants, Pattern Recognition 41 (1) (2008) 240–249.

[36] H. Schweitzer, J. Straach, Utilizing moment invariants and Gröbner bases to reason about shapes, Computational Intelligence 14 (1998) 461–474.

[37] A. R. Imre, Fractal dimension of time-indexed paths, Applied Mathematics and Computation 207 (1) (2009) 221–229.

[38] P. L. Rosin, J. Žunić, Orientation and anisotropy of multi-component shapes from boundary information, Pattern Recognition 44 (2011) 2147–2160.

[39] J. Žunić, P. L. Rosin, An alternative approach to computing shape orientation with an application to compound shapes, International Journal of Computer Vision 81 (2009) 138–154.

[40] B. Lunday, A metric to identify gerrymandering, International Journal of Society Systems Science 6 (2014) 285–304.

[41] M. B. H. Rhouma, J. Žunić, M. C. Younis, Moment invariants for multi-component shapes with applications to leaf classiffcation, Computers and Electronics in Agriculture 142 (2017) 326–337.

[42] M. Storath, A. Weinmann, M. Unser, Unsupervised texture segmentation using monogenic curvelets and the Potts model, in: Int. Conf. Image Processing, 2014, pp. 4348–4352.

[43] Z. X. Yang, X. Li, J. Yang, Quantifying and modelling fabric anisotropy of granular soils, Géotechnique 58 (4) (2008) 237–248.

[44] C. J. Lintott, K. Schawinski, A. Slosar, K. Land, S. Bamford, D. Thomas, M. Raddick, R. Nichol, A. Szalay, D. Andreescu, et al., Galaxy Zoo: morphologies derived from visual inspection of galaxies from the Sloan Digital Sky Survey, Monthly Notices of the Royal Astronomical Society 389 (3) (2008) 1179–1189.

[45] L. Shamir, Ganalyzer: A tool for automatic galaxy image analysis, The Astrophysical Journal 736 (2) (2011) 141–148.

[46] N. Otsu, A threshold selection method from gray-level histograms, IEEE Transactions on Systems, Man, and Cybernetics 9 (1979) 62–66.

[47] J. Flusser, T. Suk, Pattern recognition by affine moment invariants, Pattern Recognition 26 (1) (1993) 167–174.

[48] L. Gorelick, M. Blank, E. Shechtman, M. Irani, R. Basri, Actions as space-time shapes, IEEE Transactions on Pattern Analysis and Machine Intelligence 29 (12) (2007) 2247–2253.

[49] J.-M. Geusebroek, A. W. Smeulders, J. Van De Weijer, Fast anisotropic Gauss filtering, IEEE Transactions on Image Processing 12 (8) (2003) 938–943.